IPP-Report

MAX-PLANCK-INSTITUT
FÜR PLASMAPHYSIK

Nassim Maaziz

Improving Power Balance on Wendelstein 7-X

IPP 2024-10
April 2024

Improving Power Balance on Wendelstein 7-X

Nassim Maaziz
Supervisor: Dr Felix Reimold

January-June 2021

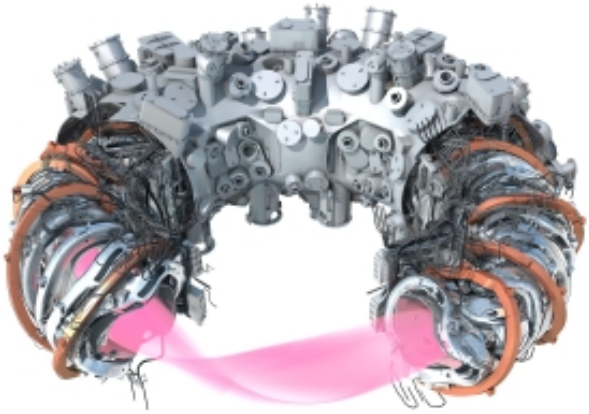

Max-Planck-Institut
für Plasmaphysik

MAX PLANCK
GESELLSCHAFT

Wendelstein
7-X

Contents

1 Introduction

Wendelstein 7-X is the largest stellarator worldwide, operated in Greifswald, Germany. The main purpose of this experiment is to demonstrate the suitability of a stellarator for a future fusion power plant. The main advantage of a stellarator-type machine compared to the Tokamak, the most promising magnetic confinement concept, is steady state operation. Following a major upgrade and starting in 2022, during the next experimental campaign the W7X team will realise quasi steady-state operation for up to 30 minutes.

In order to fulfill its mission, W7X should enable stellarator physics and technology to be pushed forward. Encompassing higher performance stellarator plasmas than ever achieved before and credible solutions for power exhaust. The latter point is tackled through the operation of an island divertor, which should ensure power exhaust at the edge while preserving the performance in the core.

The material heat flux limitation of $10MW.m^{-2}$ on the divertor targets of future reactors leads to the need of exhausting a major part of the power through radiation, this guarantees a heat deposition on a larger area and thus reduces the heat flux on the targets. The risk of target melt down can in this so-called *detached* regime be controlled. Detachment experiments have successfully been carried out during the last campaign in Wendelstein 7-X.

Energy is injected to heat the plasma through electromagnetic waves and neutral beams, the energy is partly stored in the plasma and partly flows out of the plasma through radiation deposited on the whole plasma vessel and convection to the targets. This balance is monitored over time and leads to a power balance. The input power, which sums up the power injected through electromagnetic waves at the electron cyclotron resonance frequency (ECRH) and the neutral beam injection (NBI) is identified as heating power: P_{heat}. It is balanced out by the power radiated P_{rad} and the power at the targets measured by infrared cameras: P_{IR}. Let's call W the stored energy in the plasma. The power balance reads:

$$P_{ECRH} + P_{NBI} = P_{heat} = P_{rad} + P_{IR} - \frac{dW}{dt} \tag{1}$$

However, this balance does not hold when looking at the measurements. There is sometimes too much power flowing out, and other times not enough. This work focuses on understanding this inconsistency of the power balance and ways to improve it. The analysis is here performed on P_{rad}, the measured radiated power and P_{IR}, the power to the targets. Due to time constraints, P_{heat} is not studied.

First, trends in the power balance deviations are examined and visualised through a database of plasma discharges. In a second part, the measurement of P_{rad} are assessed from a geometrical point of view. Part of this radiated energy is deposited on the targets and is counted on top of the convection contribution by the IR cameras; a third step is dedicated to studying this phenomenon's impact on the power to the targets.

2 Database

2.1 Correction factor f_{cor}

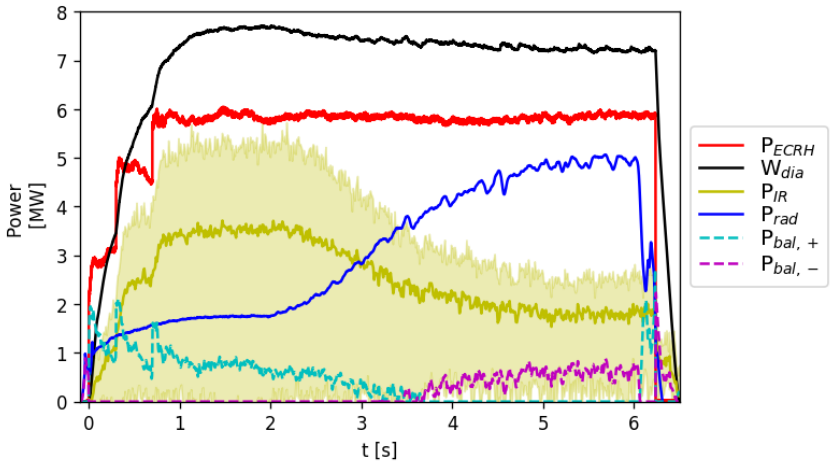

Figure 2: Discharge: 20181016.9

Figure 2 displays a shot where it is possible to observe the deviation from balance with the two terms $P_{bal,+}$ in cyan and $P_{bal,-}$ in magenta. The first term represents the input energy which is not accounted for, the second one is none-zero when too much energy is measured, this is not physical and could mean that part of the input energy is counted twice in the output sum. This last possibility is supported by a higher part of the radiated power at the end of the discharge: when $P_{bal,-}$ grows.

As explained above, P_{rad} is here the parameter of interest in the power balance. A coefficient: f_{cor} is added to equation (1) to evaluate the needed correction for the power balance to hold. The equation now reads:

$$P_{ECRH} + P_{NBI} = f_{cor} \cdot P_{rad} + P_{IR} - \frac{dW}{dt} \tag{2}$$

Figure 3 displays the same discharge but this time $f_{cor} = 0.75$. This implies that a quarter of the measured radiated power is not considered anymore. It is similar as stating: "25% of the radiated power ends up on the target". The consequence is the suppression of the unphysical additional power: the magenta line stays at 0.

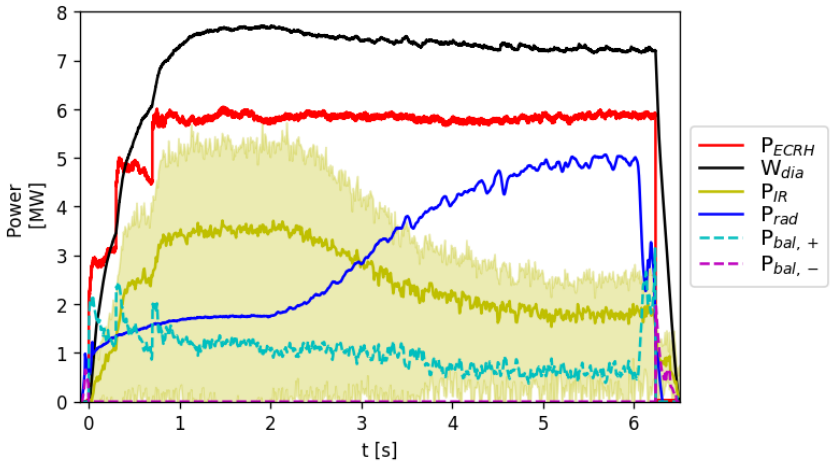

Figure 3: Discharge: 20181016.9 - $f_{cor} = 0.75$

It appears quite clearly that there is no unique value of f_{cor} for which the power balance holds. To study the parameters influencing this coefficient, the power balanced is assumed to be held in equation (2) so that the coefficient f_{cor} needed for this balance to hold is calculated at every time point. The equation becomes:

$$f_{cor} = \frac{P_{ECRH} + P_{NBI}}{P_{rad} + P_{IR}} \tag{3}$$

To identify robust trends in the evolution of f_{cor}, steady state conditions are preferred, transients are excluded. The change in the plasma stored energy has been thus left out of this formula.

2.2 Trends

The correction factor can be first thought to respect: $f_{cor} \in [0; 1]$. It must be lower than 1 when subtracting the energy deposited on the targets. However, in some shots, the correction factor exceeds 1, which means that too little output power is measured. There are uncertainties on every measurement, not only in P_{rad}, these uncertainties could partly explain this phenomenon.

Toroidal asymmetries could also explain an underestimation of the measured radiated power: when radiation is not the dominant exhaust mechanism, the radiation is located closed to the interaction zones: the divertor targets. The measurement of the radiation is so far done on another toroidal location, further away from the interaction zone of the plasma with the targets. In this situation, the radiation at the measurement plane might be lower than the average and induce an underestimated extrapolation to the whole plasma.

Figure 4a shows the previously presented discharge (20181016.9). The time evolution of the quantities of interest is above and below this is the evolution in time of the parameter f_{cor}.

The first observation is that f_{cor} is lower than 1 for a high radiation fraction. So there is too much energy flowing out of the system, potentially implying double counting. This radiation fraction is defined as the amount of power radiated with respect to the heating power:

$$f_{rad} = \frac{P_{rad}}{P_{heat}} \tag{4}$$

It is first assumed that the correction factor is only f_{rad}-dependent. At high radiation fraction, it seems that the radiation power is overestimated as f_{cor} is lower than 1. Part of the power is deposited on the targets, this fraction of the radiated energy seems to reach approximately $15 - 20\%$: one can observe on Figure 4 a value of f_{cor} between 0.8 and 0.85 for high radiation fractions during steady state conditions at the end of the discharge. Next chapter will investigate geometrical considerations which could also lead to a misestimation of P_{rad}.

There is no clear explanation for the high f_{cor} at low radiation fraction and high IR power. The above mentioned toroidal asymmetry effect is to be verified. During the next experimental campaign, a new bolometry system, located in the divertor region will enable to assess possible variations between the measurements in the triangular plane, current only radiation measurement

location and the divertor region. It will allow for a better estimation of the radiated power for a low radiation fraction but also testing the toroidal symmetry assumed at higher f_{rad}.

Figure 4b shows a discharge (20181016.11) with a similar evolution of the radiation fraction. For this shot, the values of f_{cor} are similar to the previous example: around 1.5 when little radiation is detected and around 0.85 for a high radiation case. It could seem like for steady state time intervals, there is a range of values of f_{cor} which solves the deviation from power balance.

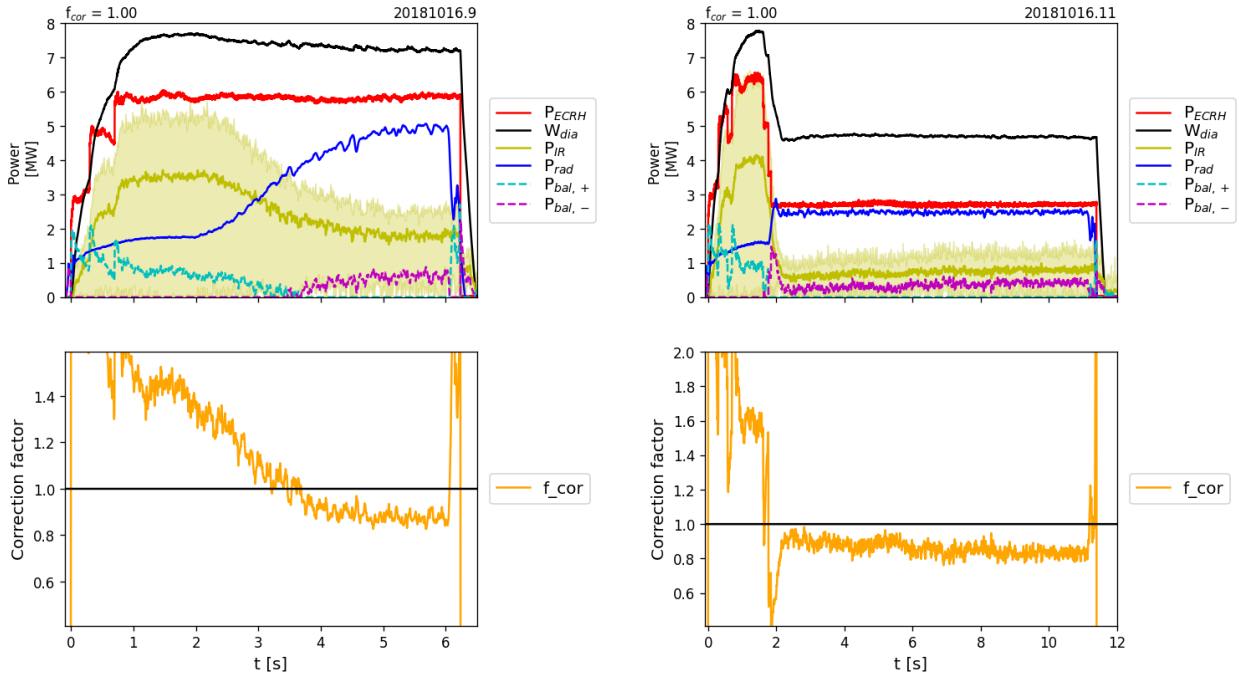

(a) Discharge 20181016.9

(b) Discharge 20181016.11

Figure 4: Evolution of f_{cor} for two similar discharges

Figure 5 shows two other discharges (20181010.34 and 20180920.46). At the end of the discharges, the radiation fraction is high, and f_{cor} lies also around 0.8. However, there is a major difference in these shots, during the first part, for a low f_{rad}, f_{cor} is lower than 1.

Modeling suggests that there is a relative toroidal symmetry of the radiation only for a high radiation fraction. The toroidal symmetry of the radiation is a strong assumption on which the rest of the study is built. Therefore, only deviations from power balance for high radiation fraction will be considered.

This excludes *de facto* to try to understand the difference between f_{cor} in Figure 4 and in Figure 5 for low f_{rad}.

It is interesting to test to go beyond the single f_{rad}-dependence of f_{cor}. In order to look more closely into the driving parameters of f_{cor}, a database of a few shots has been built. This database enables to plot a few parameters in function of others in the form of scatter plots to look for correlations between them.

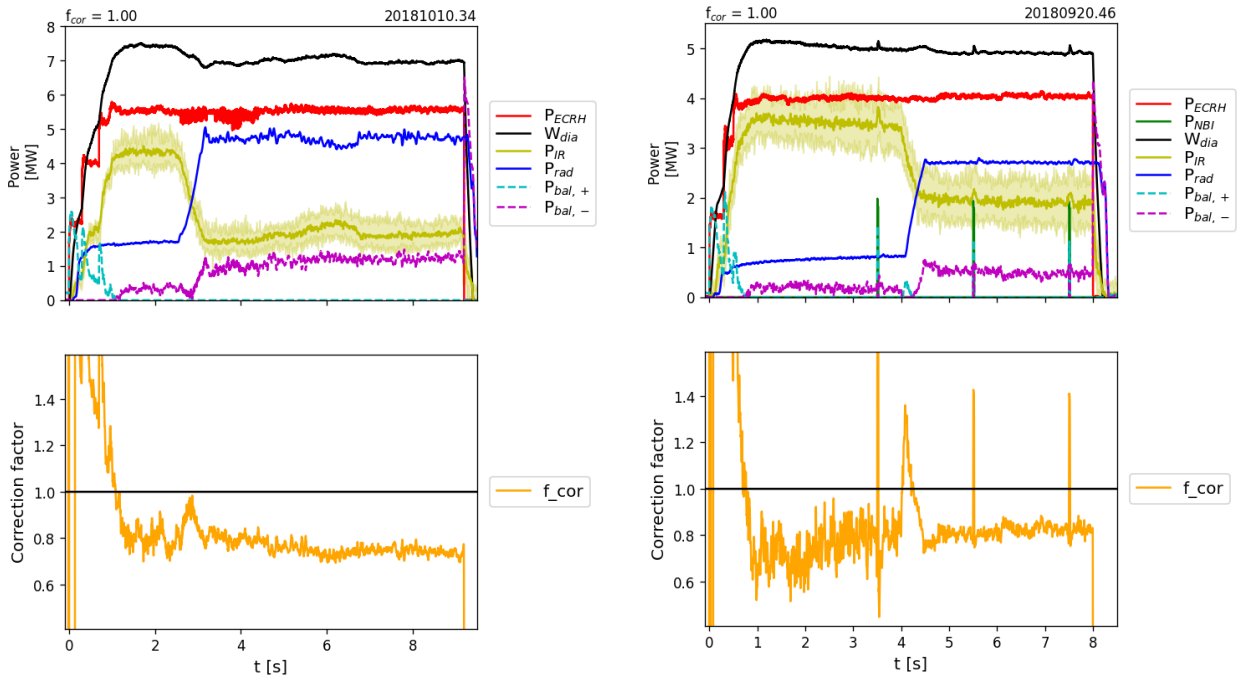

(a) Discharge 20181010.34

(b) Discharge 20180920.46

Figure 5: Evolution of f_{cor} for two discharges which display a different behavior

2.3 Scattered plots

A collection of values of f_{cor} have been plotted against other parameters in order to visualize the evolution trends. It appeared no direct correlation between f_{cor} and the density n_e or between f_{cor} and the heating power, mostly P_{ECRH}. The previous assumption about a correlation between f_{cor} and f_{rad} has been confirmed. Figure 6 shows f_{cor} against f_{rad}. It describes decreasing behavior for f_{cor} with respect to an increasing f_{rad}. The more the energy is radiated, the more the correction factor decreases.

As explained above, the requirement of toroidal symmetry excludes low radiation fraction cases. When looking above $f_{rad} = 0.5$ there is a linear decreasing behavior of f_{cor} with an increasing value of f_{rad}.

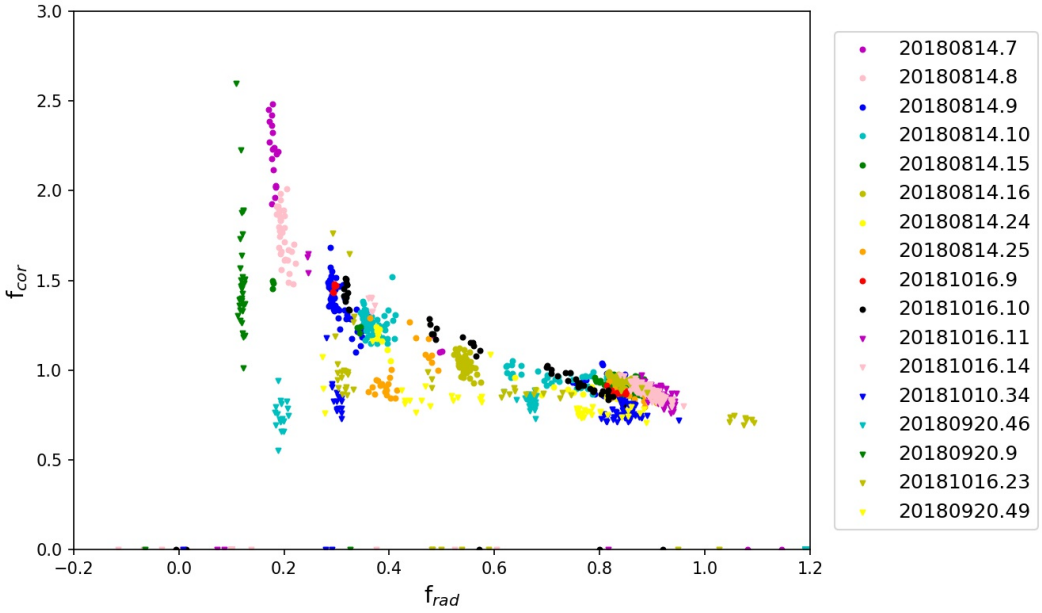

Figure 6: Scattered plot of the correction factor against radiated fraction

One can observe that for an increasing radiation fraction, the power balance correction has to be increased.

The next two chapters will investigate the links between the radiation fraction evolution on two terms of the power balance equation: P_{rad} and P_{IR}.

3 Geometric analysis of the bolometry signal

3.1 Bolometry

The radiated power is measured with bolometer cameras. Bolometers measure radiation through the deposition of the energy on a foil, usually copper or gold, the change in temperature of the system propagates and can influence the resistivity of a material, the change in resistivity is measured, this gives the change in temperature which can be linked back to the input power deposited on the foil. The stellarator Wendelstein 7-X is equipped with two bolometer cameras to measure the radiated power: the horizontal bolometer camera (HBC) and the vertical bolometer camera (VBC). They are toroidally located in the triangular plane, around 36° in the toroidal direction, with a slight toroidal angle which is here neglected (4°and 6°respectively for HBC and VBC). The measured radiated power at this location is then extrapolated to the rest of the plasma.

A 2D representation of the bolometry system at W7X at the triangular cross section is represented in Figure 7. VBC is located below the plasma, at the bottom of the vessel and looking up. HBC is at the low field side, and is directed towards the high field side.

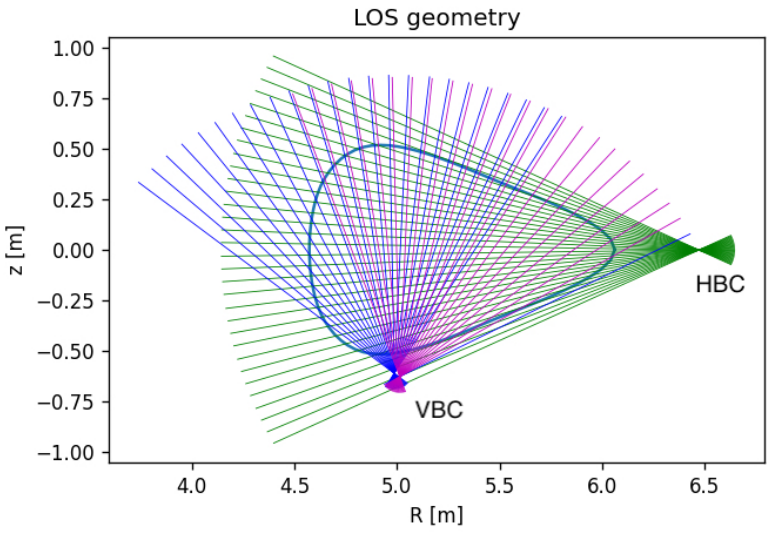

Figure 7: Schematic representation of the bolometry system

3.2 Modeling

3.2.1 P_{rad} calculations

To study the measurement of the radiated power, a radiating plasma is modeled and a synthetic measurement equivalent to what is done on W7-X is compared to the known radiated power value.

The modeling is built as follows: a radiation distribution is set on the W7-X plasma geometry, obtained via vmec flux surfaces. The plasma volume is discretized in 360 slices of constant depth. On each surface, the same radiation distribution is given: the value of the emissivity ε is field-aligned to fulfill the assumption of a radiation toroidal symmetry. So the radiation distribution is set once and assigned to every slice so that it is aligned to the magnetic field lines.

This set radiation distribution is integrated over the volume and is considered as the reference value of the radiated power. The synthetic bolometry system should reconstruct the radiated power in a similar way to what is done routinely on W7-X and be as close as possible to this value.

The synthetic bolometry system works as follows: two sets of lines of sight are set: one to model VBC and the other for HBC. When the line of sight crosses a none-zero emissivity region it multiplies the local energy density by the length of the line crossing this region, this product is then multiplied by a characteristic area corresponding to the cross section of the line of sight. This is done over all the line of sights and results in a measurement of the radiated energy by the system. This energy is divided by the volume of the lines of sight in the plasma, giving back an averaged emissivity. This last value is scaled up by multiplying by the plasma volume. This scaled up power is the estimate of the radiated power in the whole plasma vessel. The process performed in this synthetic diagnostics is reproducing the actual P_{rad} measurement at W7-X.

The main goal is thus to reconstruct the radiated power, based on measurements on the triangular plane only and scaled up, and to compare it with a computed radiated power where the radiation is 3D integrated to give a reference value of the radiated power. A deviation between both could explain the gap to power balance as it would imply a poor measurement of the radiation term. Moreover it could quantify the deviation from the measurement with respect to the actual value, known by integrating. It could also give a trend on the deviation magnitude in function of parameters such as f_{rad}.

It has been observed in last part that f_{cor} is dependent of f_{rad}. So it is of interest in this chapter to vary f_{rad} and observe the behavior of the deviation of the reconstructed radiated power compared to the reference.

An increasing deviation means a decreasing quality of reconstruction. This latter phenomenon would identify the P_{rad} measurement as a source of error in the power balance.

Moreover, varying the radiation level has independently been observed to change the radiation distribution. This comes from tomographic inversions and gives additional information on the radiation distribution to set in the model, allowing to assess the quality of reconstruction with f_{rad} as an input parameter and the radiation distribution as an intermediate step. This study has thus been performed with different radiation distributions, corresponding to different levels of radiation fraction. The goal is here to assess if the P_{rad} measurement is radiation distribution dependent and if this dependence can shed some light in the deviation from power balance.

3.2.2 Radiation distribution

This paragraph aims at present and justify the radiation distributions used in these forward calculations.

First of all, the emissivity is set to be 1 $W.m^{-}3$ over the whole cross section. The reconstructed and computed power are supposed to be equal as the bolometer scale to the plasma an averaged emissivity which has to be the right one in this homogeneous situation. This distribution is referred to as case I and is shown in Figure 8a.

A second distribution, case II, shown in 8b is chosen to set the radiation only in the plasma edge. This is the region where most of the radiation is emitted in the experiments. In this situation a deviation could already appear as the emissivity can be reconstructed poorly by the bolometry system.

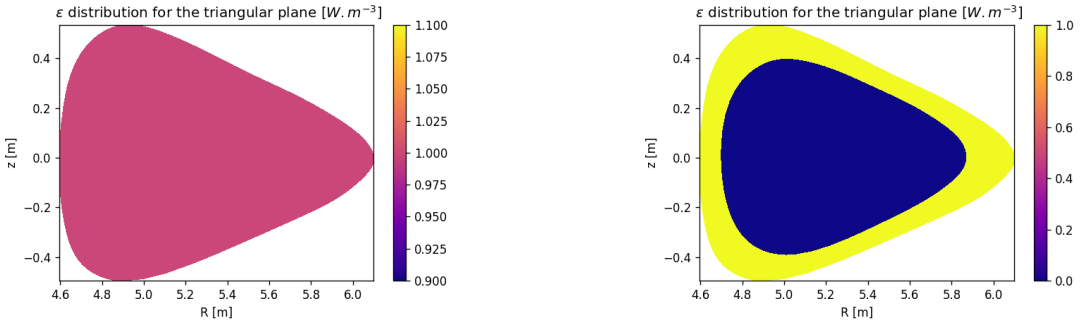

(a) Radiation distribution: case I

(b) Radiation distribution: case II

Figure 8: Evolution of f_{cor} for two discharges which display a different behavior

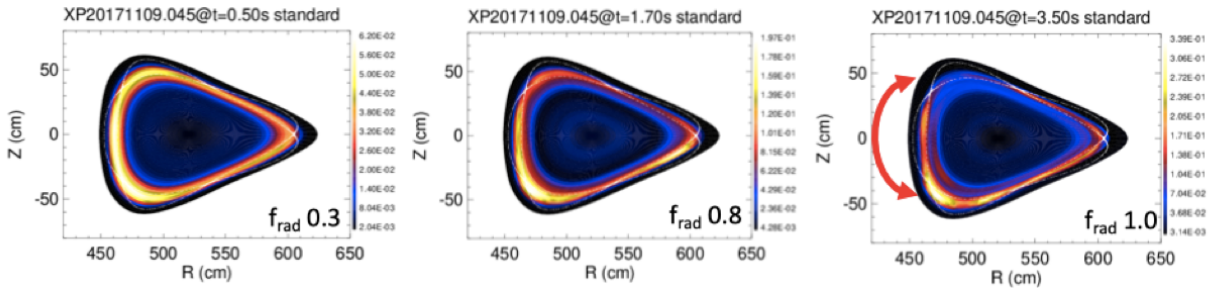

Figure 9: Radiation distribution in function of the radiation fraction

The next radiation distributions chosen in this study are based on tomographic inversions. The bolometers measurements from the experiments were used to reconstruct the radiation distributions on the triangular plane. This additional information on the typical radiation distribution and on its evolution are used to assess how the geometrical distribution can affect the magnitude of the radiated power measured by the bolometers.

The link, previously established between the radiation fraction and the correction needed for the power balance to hold is further explored by using radiation distributions corresponding to different level of radiation fraction, and quantifying the quality of reconstruction with this increasing radiation fraction by applying the corresponding radiation distribution to the synthetic diagnostic. For a given f_{rad}, the radiation distribution is found based on the inversions.

In Figure 9, the radiation distribution on the triangular plane has been calculated through tomographic inversion for different radiation fractions, based on experimental measurements. These distributions evolve with an increasing radiation fraction: the higher it gets the more the radiation moves towards the bottom part of the cross section. There is a bottom-up asymmetry build up.

Considering these inversions, case III of the radiation distribution simulates a radiation fraction of $f_{rad} = 0.5$ whereas case IV assumes a radiation distribution for $f_{rad} = 1.0$. See Figure 10a and 10b.

In the case of a good reconstruction, for every radiation fraction, leading to various radiation distribution, the radiated power calculated by the bolometers on one plane is equal to the radiated power 3D integrated. A ratio of both quantities is a measurement of the quality of the measurement and is used in what follows as the quantification of this quality.

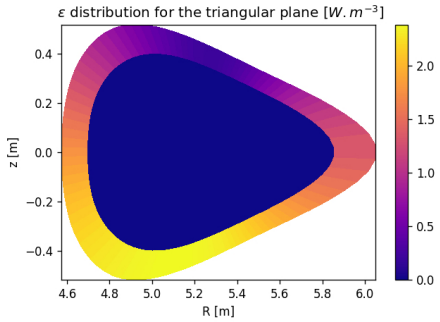

(a) Radiation distribution: case III

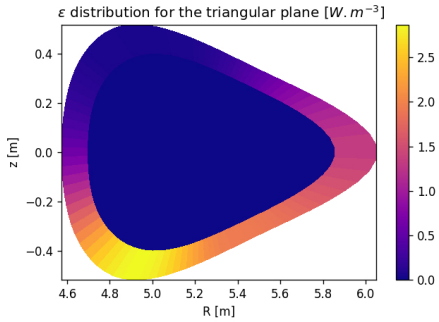

(b) Radiation distribution: case IV

Figure 10: Evolution of f_{cor} for two discharges which display a different behavior

3.3 Results

The results in assessing the quality of the reconstruction is given in the form of the ratio R, defined as the power reconstructed by the synthetic diagnostic, which simulates the value of P_{rad} measured by the bolometers, divided by the computed value of P_{rad}, which is the actual radiated power in the vessel as it integrates over the volume the energy density applied in the simulation:

$$R = \frac{P_{measured}}{P_{calculated}} \tag{5}$$

Table 1: Quality of the reconstruction in function of the input radiation distribution

Case number	R_{HBC} [-]	R_{VBC} [-]	Info
case I	1.0	1.0	Homogeneous
case II	0.91	1.09	Edge Radiation
case III	1.05	1.15	$f_{rad} = 0.5$
case IV	1.1	1.3	$f_{rad} = 1.0$

For high radiation fraction, P_{rad} is overestimated. The ratio is 1.3 for VBC and 1.1 for HBC when looking at the radiation distribution corresponding to high radiation fraction. This is equivalent to an overestimation of respectively 30% and 10%. When f_{rad} is divided by 2, the overestimation seem to be

approximately divided by 2. The linear relation previously observed in Figure 6 is thus retrieved.

3.4 Source of errors

In order to try to understand the source of errors in the reconstruction as done on W7-X, two different phenomena are identified and explained in this paragraph.

3.4.1 Line of sight density

The first one is the line of sight density, when closer to the camera, a region has a bigger impact on the measurement. To represent this varying line of sight density on the triangular plane a map is shown in Figure 11a for the HBC camera and in Figure 11b for the VBC camera. The plotted parameter is the ratio of the line of sight density in a cell used to discretize the cross section, divided by the mean line of sight density.

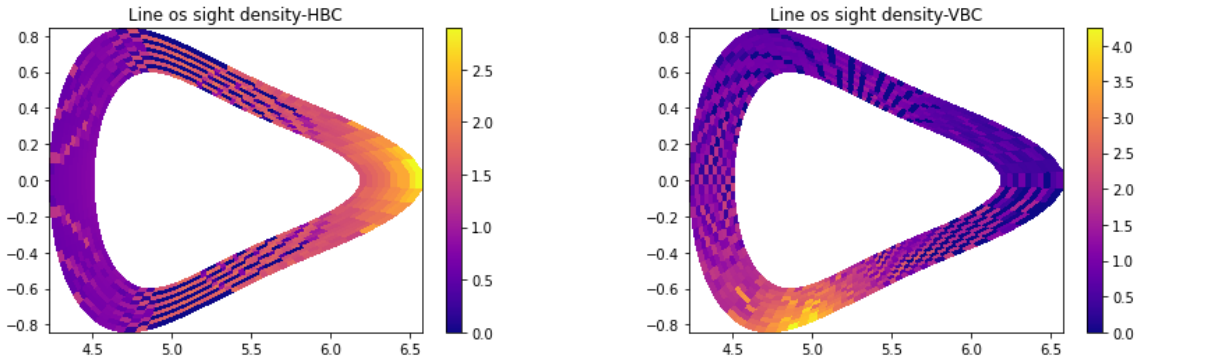

(a) Line of sight density effect for HBC (b) Line of sight density effect for VBC

Figure 11: Line of sight density effect

For each cell, the numerator is the total length of all the lines of sight crossing the cell boundary, divided by the cell area. The denominator is the same for every cell and is the total length of all the lines of sight crossing the boundary of the plasma cross section, divided by the area of the triangular cross section.

It is obvious that closer to the camera the values are higher than the mean value, whereas the values are lower than the mean further away.

This contributes to the error in the reconstruction as performed on W7X by giving a higher weight to the emissivity in certain regions than in others.

In other terms, if the radiation lies in a dense line of sight region of the cross section, the total amount of radiation will be overestimated, whereas is will be underestimated if the radiation is located in a region where there is less line of sight. This comes from the fact that the average emissivity, before to be scaled up is calculated by multiplying along every line of sight ε by an infinitesimal line of sight volume: $dldA$. The value of ε in a region with a lot of line of sights will be multiplied many times by these many line of sights. The opposite happens for the emissivity in a region with less line of sights.

3.4.2 Volume representativity

The other source of error is the representativity of the volume of the cells in the triangular plane region when compared to the contribution of the same region but averaged over the whole toroidal direction along the magnetic field line.

In more details, every cell is given a power density, the power density is multiplied by the infinitesimal volume of the line of sight. The bigger the cell the bigger the more line of sight it sees the bigger the impact on the total radiated power. The area of every cell in the triangular cross section is thus a parameter of importance. Every area is multiplied by an incremental depth, corresponding to distance between the cross sections, apart from 1° in the toroidal direction, to give a volume to the cells. This paragraph deals with volume representativity but as every area is multiplied by the same depth, the comparison will be done between the areas.

As previoulsy said, each cell has an area and this area determines the weight of the cell in the triangular cross section and the reconstruction routinely done on W7X uses data from only this toroidal location. Therefore is makes sense to verify that the area of a cell at the triangular plane is representative of the other cross sections. The radiation is field aligned: each of the 4 corners of a cell is traced along the magnetic field lines, this deforms the cells. As a matter of fact, some cells have at the triangular cross section an area which is larger or smaller than it should when considering the others cross sections. To perform this comparison, every cell area is averaged toroidally: the 360 areas of the same cell but at different toroidal locations are summed up and normalized by 360. The area of the cell at the triangular plane is divided by the corresponding mean area and this ratio gives a map presented in Figure 12.

It appears that the left and right regions have a bigger area in this cross section than their respective toroidal mean. The top and bottom regions are not very well representative of the area: these cells have a smaller area than

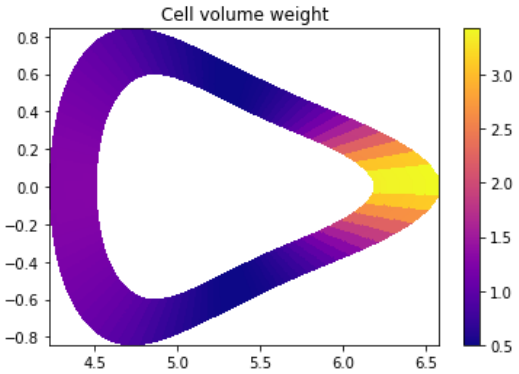

Figure 12: Cell volume effect

they should have when considering the whole toroidal extent.

In this sense the radiation located in the top and bottom parts are underestimated whereas the radiation on the low field side of the machine is overestimated by a non negligible amount, the high field side region is also overestimated.

3.5 Comparison to experimental measurements

Being able to quantify the deviation and link it to a parameter such as f_{rad} suggests that it's possible to correct back the measurement of the radiated power.

In a second step, to gain confidence on the modeling performed above, a correction has been applied to a data set of experimental measurements.

Figure 13 presents the value of the radiated power measured by the bolometer VBC in function of the same parameter P_{rad} but this time measured by the HBC camera. Both sets are normalized by the heating power P_{heat}. This results in a graph presenting the radiation fraction measured by VBC in function of the radiation fraction measured by HBC.

Steady state conditions are considered: the energy stored in the plasma is constant. This implies $f_{rad} \in [0; 1]$. Because it is only possible to radiate between 0: all the energy goes to the targets without radiation and 1: at each time, all of the heating power goes out as radiation. It is also expected that both measurements are the same as they measure the same physical quantity. Thus the points should be located in the bottom left corner to respect $f_{rad} < 1$ and on the line $y = x$ as it's the same physical quantity which is being measured.

Figure 13 shows that the majority of the points are above the $y = x$ line

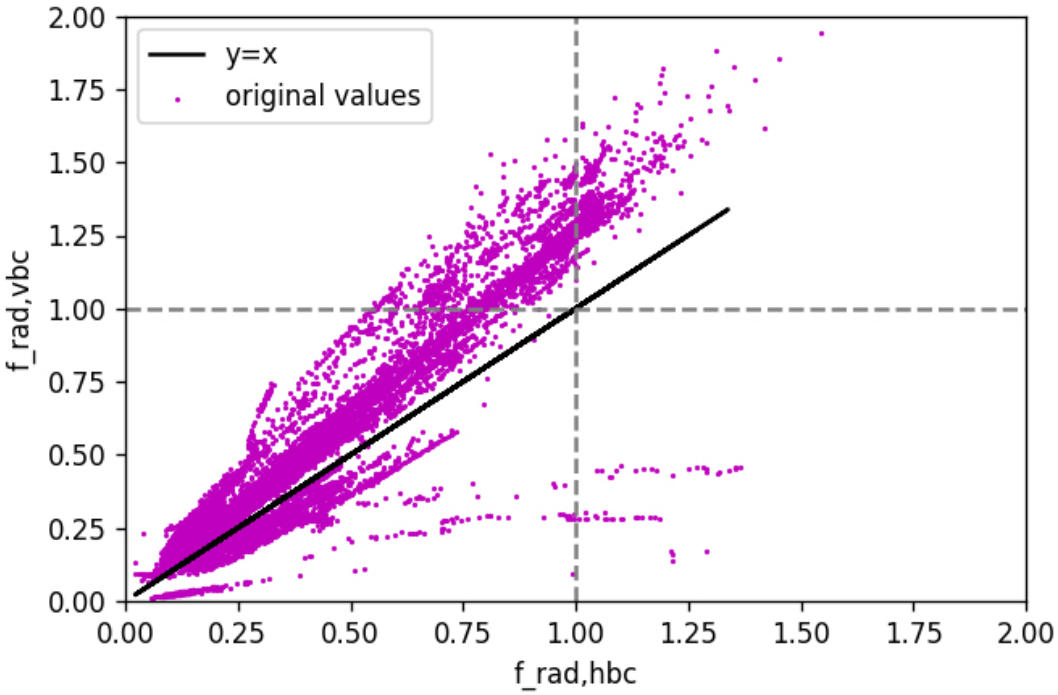

Figure 13: Experimental data points: Radiation fractions of VBC in function of HBC

and that a large number of points are not contained in the bottom-left corner as it should.

These same points are corrected to account for the overestimation found in the modeling part. It has been observed that the overestimation of 30% for VBC and $f_{rad} = 1$ is 15% for $f_{rad} = 0.5$. For HBC the 10% overestimation goes down to 5% for half of the radiation fraction.

This linear relationship is used to correct back the measurements for all f_{rad}: from the original line in magenta, every point is scaled down by a factor which depends itself on the value of f_{rad}.It should be the same for $f_{rad,old} = 0$ and divided by 1.3 when the old value is $f_{rad,old} = 1$:

$$f_{rad,new,vbc} = \frac{f_{rad,old,vbc}}{1 + 0.30 \times f_{rad,old,vbc}} \tag{6}$$

And similarly for HBC:

$$f_{rad,new,hbc} = \frac{f_{rad,old,hbc}}{1 + 0.10 \times f_{rad,old,hbc}} \tag{7}$$

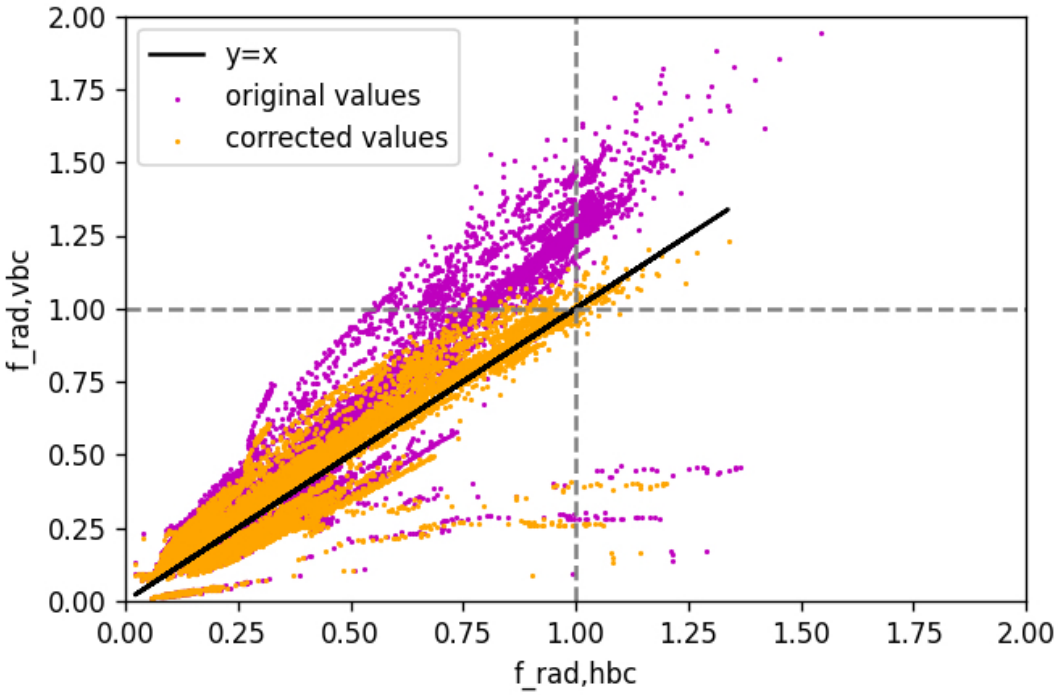

Figure 14: Experimental data points and the corrected points: Radiation fractions of VBC in function of HBC

Figure 14 shows a better arrangement of the radiation fraction points. The vast majority follow $f_{rad} \in [0; 1]$ and are grouped along the $y = x$ line. This means that the measurements are both physical and similar.

It is important to state here once again that this back correction has been performed with inputs coming from the results of the modeling explained above. The values of 30% and 10%, as well as the approximation of a linear behavior have not been derived to fit the point cloud but have been confirmed to be reasonable approximations by this back correction.

4 Target heat loads

This part will focus on the second term of interest: P_{IR}. It stands for the power measured by the IR camera on the divertor plates. This is the contribution to the power flowing out of the plasma corresponding to the convection flux of hot particles, originating in the core of the plasma and flowing out towards the divertor. The resulting heat flux is restricted to $10MW.m^{-2}$ to prevent the melting of the plates.

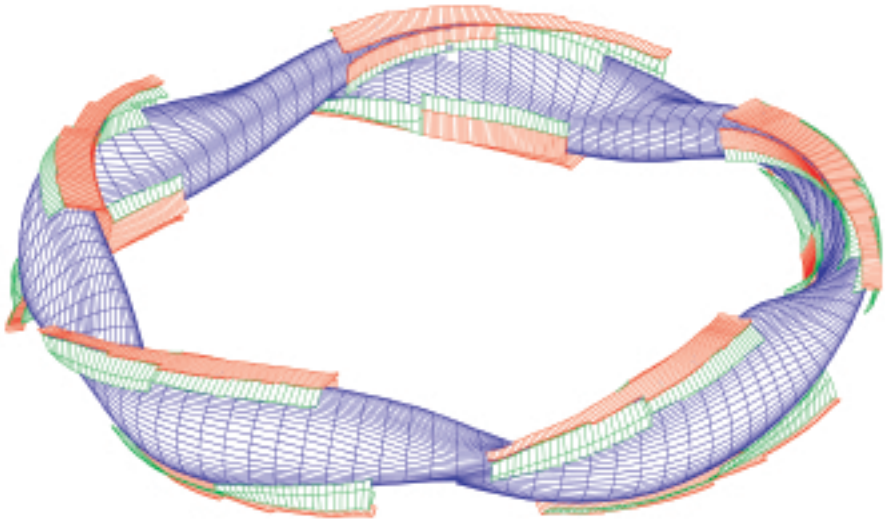

Figure 15: Wendelstein 7-X plasma, divertor and baffles

The interest of this chapter is to quantify the contribution of the radiated power on the divertor plates. This phenomenon leads to a double counting of the radiated power as it is measured by the bolometers first, but also by the IR camera when the energy is deposited on the targets. The evolution of this double counting in function of an increasing radiation fraction is conducted in this part as well. The identified trends will be considered as the contribution of the term P_{IR} to the deviation from power balance and its evolution for an increasing radiation fraction.

4.1 Targets

The divertor of Wendelstein7-X consists of 5 pair of segments placed along the toroidal direction and crossing the plasma cross-section at a particular location: in the islands. On Figure 15 one can see in blue the plasma, in red, the divertor plates and in green the baffles.

The heat loads calculations are done with a ray tracing tool: *CHERAB*. Two sets of targets have been used. First the divertor targets and the baffles have been loaded from the componentsDB of Wendelstein 7-X and used for the simulations.

In a second step, the targets used for the modeling on the code emc3 have replaced the previous ones. The usage of this second set of targets simplifies the comparison between the emc3 modeling and these simulations. Moreover, this mesh being lighter, it lowers the computational cost of the simulations. Figure 16 shows a pair of divertor and baffle segments, these are downloaded from the componentsDB.

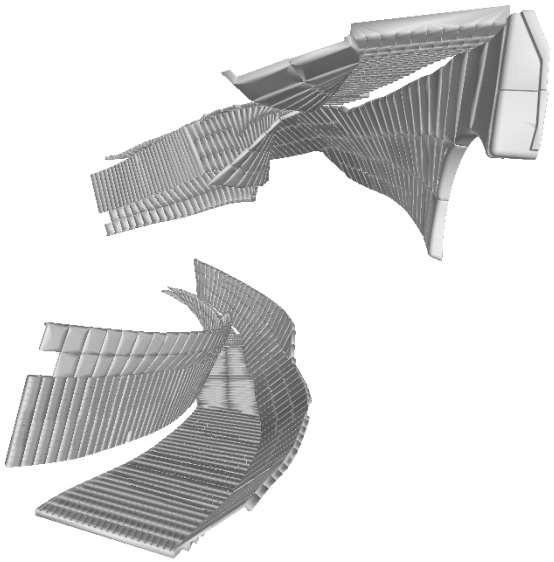

Figure 16: Wendelstein 7-X divertor and baffles

4.2 Radiation distribution

The heat loads calculations are here only due to the radiation on the targets. The interest is to quantify the proportion of the total radiation which ends up double counted because on the targets.

The radiation has been meshed as filaments, which would emit over 4π. Each filament of this radiation distribution simulates a point radiation on a specific location of every poloidal surface and is in this regard field-aligned. The radiation distribution is based on experimental and simulation observations. In a similar way as done previously, the radiation fraction f_{rad} is used as an input variable to identify the contribution of P_{IR} to the deviation from power balance, through the presence of double counting in this term.

It has been observed that the radiation is mostly located around the strike-line for a low radiation case, here approximated by an O-points radiation, increasing the radiation fraction induces a movement of the radiation towards the X-point.

The two scenarios have thus been chosen as first approximations to model the deposition of radiated energy on the divertor plate for a ramp up of the radiation fraction. As an intermediate case, the radiation is set approximately in between X-points and O-points and is arbitrarily called I-points.

The three radiation scenarios are shown in Figure 17. The blue diamonds represent the five X-points. The red circles are the five O-points. The green crosses indicate the so-called I-points (for intermediate), placed in between the X-points and the O-points.

A zoom on the lower divertor and the filaments is shown in Figure 18.

4.3 Results

The share of the deposited energy on the targets to the total radiated energy is presented for each scenario in Table 2. Values between 15% and 20% seem to be in agreement with what has been observed first when calculating f_{cor} so that the power balance would hold. The range of f_{cor} was indeed $0.80 - 0.85$.

Table 2: Share of the deposited radiation energy on the divertor plates

‘Radiation scenario	O-points	I-points	X-points
Share of the power to the target	19.5	15.6	14.9

The heat loads on the 3D divertor plates for the three radiation scenarios are shown in Figure 19.

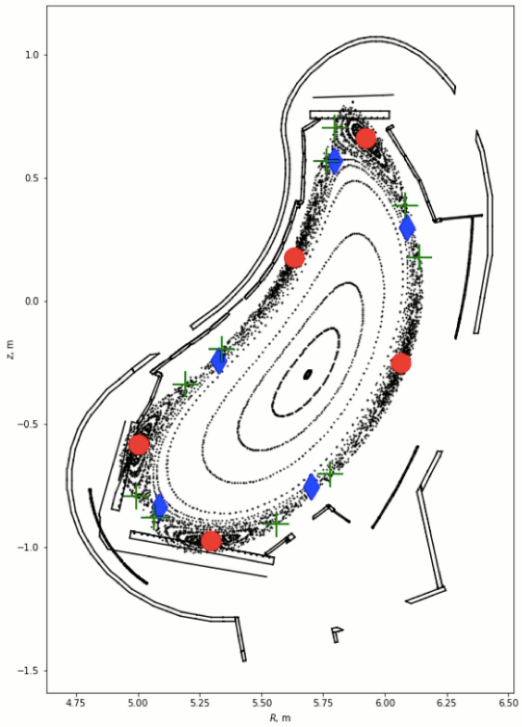

Figure 17: Three different radiation scenarios

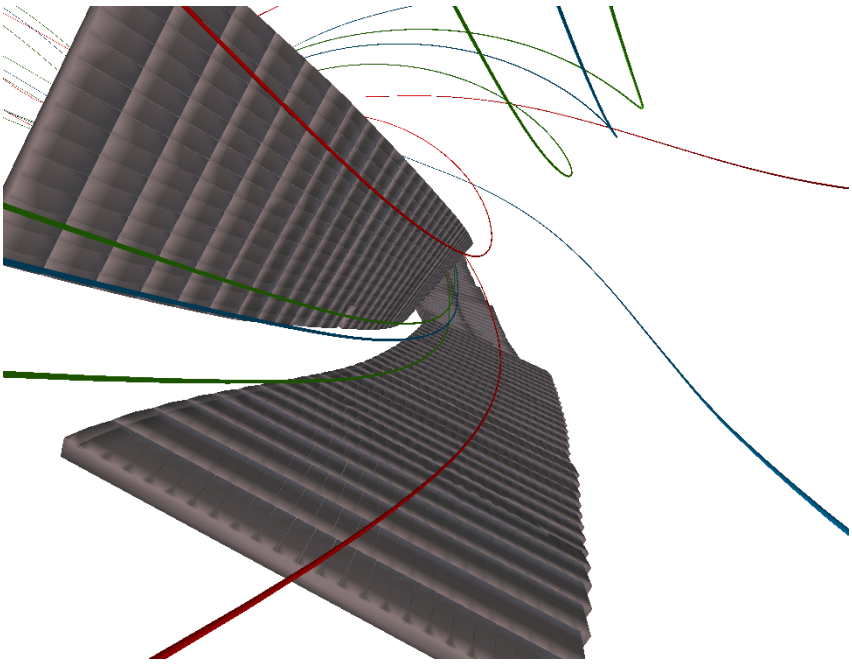

Figure 18: Lower divertor plate and radiation filaments

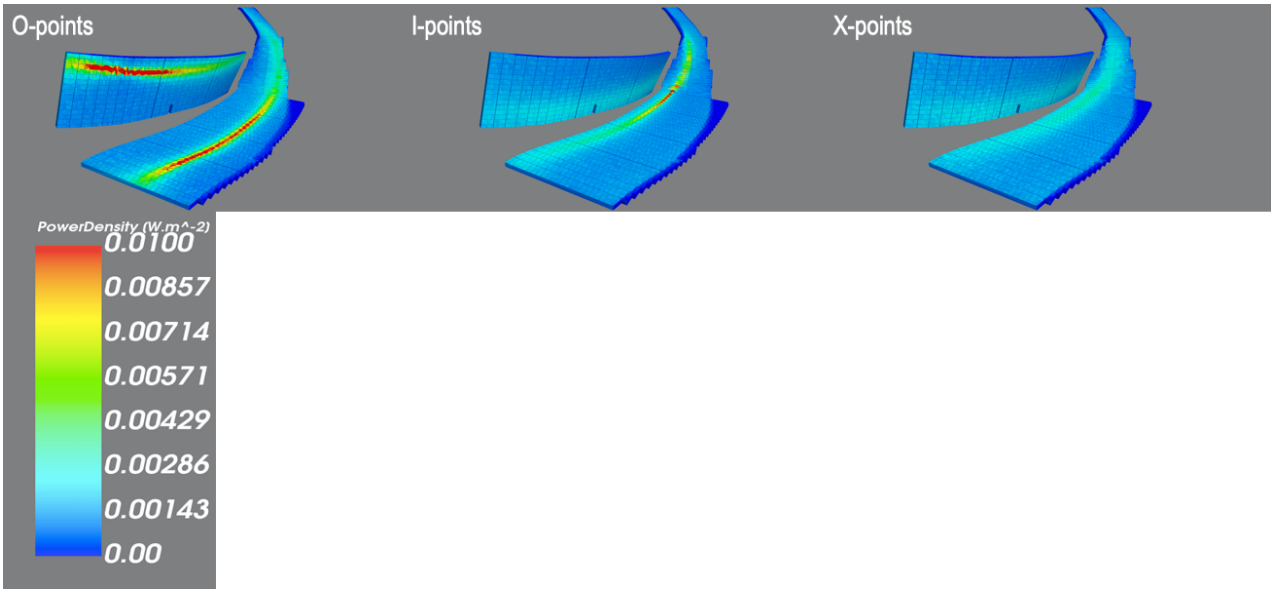

Figure 19: Heat loads on the divertor targets due to radiation

One can observe that the peak of the radiation is not located at the same location. From the X to the O points it moves towards the exterior. At the same time is also looks like the heat deposition is increasingly peaked when going from the X-points to the O-points.

Both observations are seen in Figure 20 which shows a profile of the heat deposition on the 28th finger of the horizontal plate.

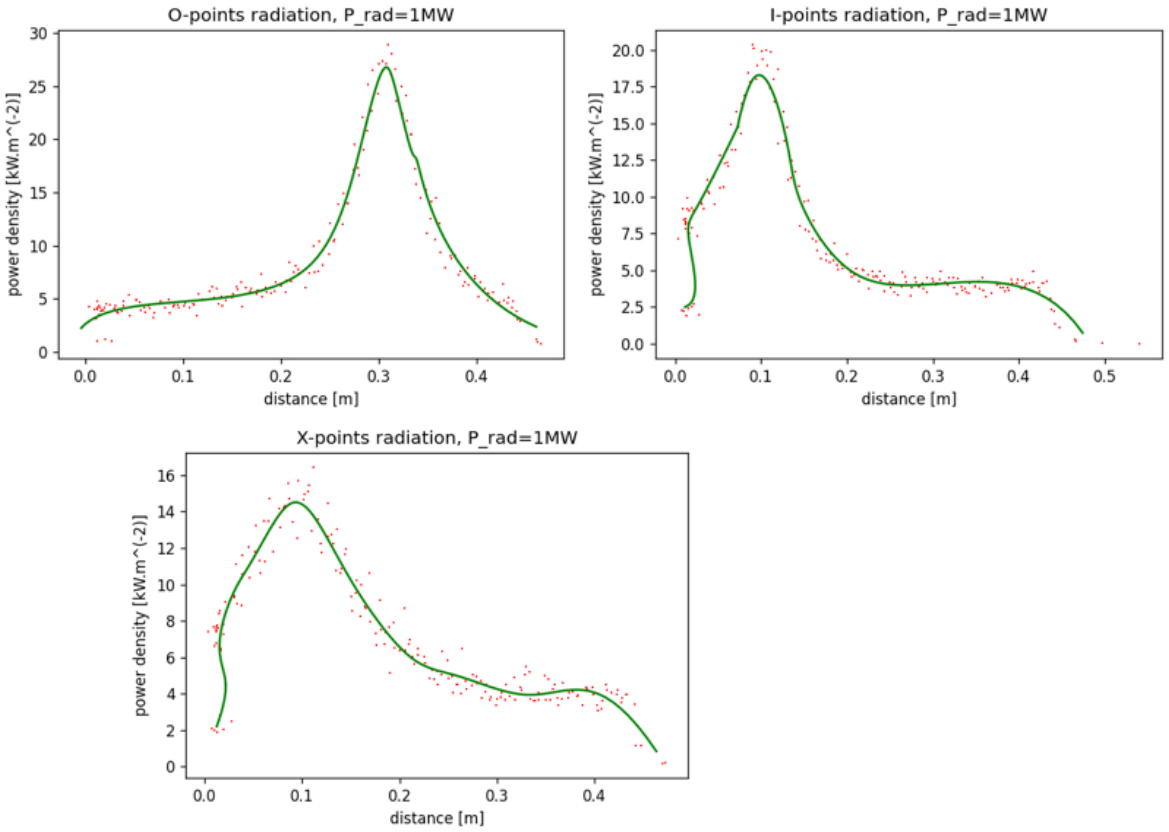

Figure 20: Profiles of the heat load deposition

5 Conclusion

This work investigates the deviation from power balance in the stellarator Wendelstein 7-X, due to limitations on the radiation measurements and the double counting of output power. Corrections seem to be needed to enhance the quality of the power balance in the experiments, these corrections can reasonably be thought to be dependent on the radiation fraction. The first part allows to grasp the complexity of this multi variable problem and gives insights on the relevant parameters of interest. The geometry of the situation is tackled in a second phase, revealing source of errors and suggesting corrections. Finally, the heat loads caused by radiation on the divertor targets are assessed and contribute to the big picture by quantifying the share of the deposited energy on the divertor.

Parts 3 and 4 are consistent with an overestimation of the power flowing out of the plasma for high radiation fractions, which has been observed in part 2. More than qualitative agreements, the two analysis led to quantitative estimates of deviation.

This work on the reconstruction of the P_{rad} signal suggests an improvement on the current measurement based on new observations. The tomographic inversions have shed some light on typical radiation distributions which in a second step can be used to correct back the first measurements.

The assessment of the share of power deposited on the divertor gives an estimate of the coefficient which could be apply to prevent double counting of some power.

These estimates consist of first approximations towards correction coefficients: many improvements are still needed to ensure power balance.

Many approximations have been made. The number of shots in the first database is too little and only gives hints on the tendencies. For the second part, a simplified 2D geometry is considered for the bolometry system and the model for the synthetic diagnostic could be refined. When considering the heat loads on the divertor it is clear that the radiation distribution can also be improved by increasing the resolution of the emitting grid.

A refined analysis could make possible a more precise estimation of the different measurement error bars and suggest better corrections. In this sense, the quest of power balance is actually a way of assessing the accuracy of diagnostics.